**TABLE 3. Comparison between 8-mAs, 16-mAs, and 32-mAs MBIR Versus 80-mAs FBP**

| | Normal Findings | | | Abnormal Findings | | | Other Findings | | Overall Image Quality |
|---|---|---|---|---|---|---|---|---|---|
| | Central Vessels and Airways | Peripheral Vessels and Airways | Interlobar Fissures | Nodules | GGO | ISP | Image Noise | Streak Artifact | |
| Reconstruction technique | | | | | | | | | |
| 32-mAs MBIR | 3.33 ± 0.09 | 3.50 ± 0.11 | 3.53 ± 0.17 | 3.46 ± 0.09 | 3.77 ± 0.11 | 3.44 ± 0.13 | 4.97 ± 0.03 | 4.97 ± 0.03 | 3.67 ± 0.12 |
| 16-mAs-MBIR | 3.07 ± 0.07 | 3.14 ± 0.14 | 3.27 ± 0.12 | 3.18 ± 0.10 | 3.27 ± 0.13 | 2.75 ± 0.17 | 4.93 ± 0.05 | 4.93 ± 0.05 | 2.93 ± 0.08 |
| 8-mAs MBIR | 3.07 ± 0.07 | 2.73 ± 0.18 | 2.93 ± 0.07 | 2.82 ± 0.12 | 2.86 ± 0.12 | 2.19 ± 0.10 | 4.87 ± 0.06 | 4.93 ± 0.05 | 2.63 ± 0.10 |
| 80-mAs FBP | 3.00 ± 0.00 | 3.00 ± 0.00 | 3.00 ± 0.00 | 3.00 ± 0.00 | 3.00 ± 0.00 | 3.00 ± 0.00 | 3.00 ± 0.00 | 3.00 ± 0.00 | 3.00 ± 0.00 |
| Pairwise comparison ($P^*$) | | | | | | | | | |
| 32-mAs MBIR versus 16-mAs MBIR | .179 | .047 | .243 | .108 | .005 | .002 | 1.000 | 1.000 | <.001 |
| 8-mAs MBIR | .179 | <.001 | .015 | .001 | <.001 | <.001 | 1.000 | 1.000 | <.001 |
| 80-mAs FBP | .004 | .001 | .037 | <.001 | <.001 | .023 | <.001 | <.001 | <.001 |
| 16-mAs MBIR versus 8-mAs MBIR | 1.000 | .023 | .115 | .013 | .023 | .017 | .965 | 1.000 | .028 |
| 80-mAs FBP | 1.000 | 1.000 | .243 | .576 | .333 | .983 | <.001 | <.001 | 1.000 |
| 8-mAs MBIR versus 80-mAs FBP | 1.000 | .821 | 1.000 | .805 | 1.000 | <.001 | <.001 | <.001 | .007 |

ASIR, adaptive statistical iterative reconstruction; GGO, ground-glass opacity; ISP, interlobular septal thickening; FBP, filtered back projection; MBIR, model-based iterative reconstruction.
Data are presented as mean ± standard deviation. Data of the subjective image analysis were statistically analyzed using the Wilcoxon signed rank tests with a Bonferroni correction applied for multiple comparisons. $P^*$ is a Bonferroni-corrected P value. $P^*$ value <0.05 was considered to be significant.
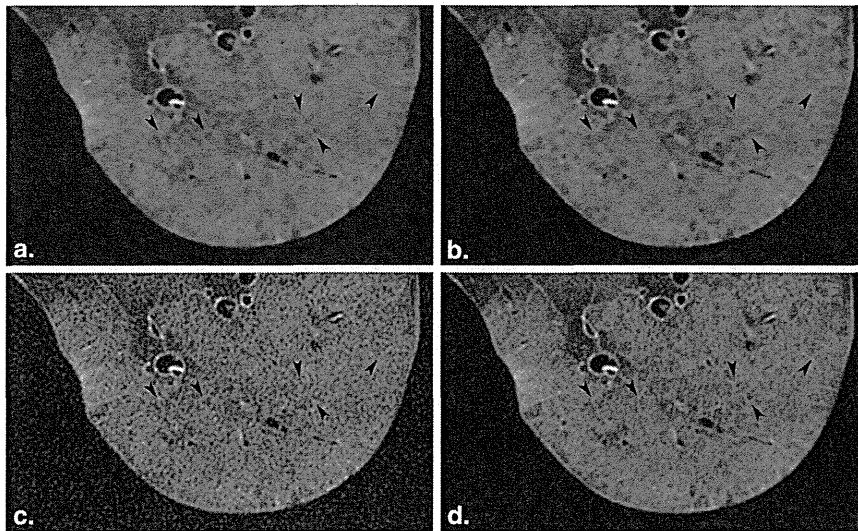
Figure 2. Thin-section computed tomographic images of a cadaveric lung with diffuse alveolar hemorrhage show diminished visibility of intralobular reticular opacities (arrowheads) on (a) 8-mAs and (b) 16-mAs MBIR images as compared to (c) 8-mAs and (d) 80-mAs FBP despite their higher noise levels. FBP, filtered back projection; MBIR, model-based iterative reconstruction.

used in scanning of the 10 cadaveric lungs are summarized in Table 1. The reported radiation dose measurements consist of CT dose index volume (CTDIvol), dose–length product (DLP), and effective dose (ED) which was calculated as the product of DLP and 'κ' conversion coefficient (0.014 mSv/[mGy cm]) for chest CT (20). Compared to standard-dose (80 mAs) technique, there were 80% and 90% decreases in dose measurements for 16-mAs and 8-mAs acquisitions, respectively with effective doses in the submillisievert range (0.31 and 0.62).

### Subjective Evaluation of CT Findings

Comparisons between images reconstructed using MBIR, ASIR blends, and FBP and acquired at 8 mAs are summarized in Table 2. Statistical analysis of four findings (consolidation, intralobular reticular opacities, cyst, and bronchiectasis) could not be performed because of their low prevalence (<2% of cases). Interobserver agreement for each evaluated category of CT findings was from moderate to excellent ($\kappa = 0.46$–1.00). There were no kappa values in the following eight items because all the same scores were graded by two observers: on MBIR images, other findings (image noise and streak artifact); on $ASIR_{30}$ images, normal findings (central vessels and airways, peripheral vessels and airways, and interlobar fissures), interlobular septal thickening, streak artifacts, and overall image quality. In each evaluated category of CT findings, MBIR scored highest with significant differences between MBIR, ASIR blends, and FBP except for interlobular septal thickening, which was not significantly different between MBIR and $ASIR_{90}$. $ASIR_{90}$ images scored significantly higher in each category than the two lower ASIR blends or FBP except for GGO, which was not statistically different from $ASIR_{60}$ ($P = .084$). Conspicuity and visibility of CT findings using $ASIR_{30}$ were equivalent to FBP ($P = 1.000$; Fig. 1). Scores

for subjective image noise and streak artifact significantly improved with increasing blends of ASIR ($P < .001$).

Comparisons between low-dose MBIR and standard-dose FBP images are summarized in Table 3. Interobserver agreement for each evaluated category of CT findings was from moderate to excellent ($\kappa = 0.42$–0.83). In each evaluated category of CT findings, 32-mAs MBIR scored highest with significant improvements in finding conspicuity, image noise, streak artifact, and overall image quality as compared to FBP ($P \leq .037$). Comparisons between ultra-low-dose (8 and 16 mAs) MBIR and 80-mAs FBP showed no statistically significant difference in conspicuity or visibility of normal and abnormal CT findings with the exception of interlobular septal thickening which was less well visualized on 8-mAs MBIR than on FBP ($P < .001$). A decrease in conspicuity of intralobular reticular opacities was identified by both observers on ultra-low-dose MBIR (Fig. 2) although formal statistical analysis could not be performed because of low prevalence of this finding. Scores for subjective image noise and streak artifact significantly improved on 8-mAs and 16-mAs MBIR images as compared to standard-dose FBP ($P < .001$), but with no significant differences among the three different dose MBIR image sets. Overall image quality was equivalent for 16-mAs MBIR ($P = 1.00$; Fig. 3) but inferior for 8-mAs MBIR ($P = .028$) as compared to FBP.

### Quantitative Image Noise Measurements

Figure 4 shows sequential and statistically significant decreases ($P < .001$) in objective image noise on 8-mAs images reconstructed with FBP, increasing blends of ASIR and MBIR. Figure 5 similarly shows sequential and statistically significant decreases ($P < .001$) in objective image noise on images acquired and reconstructed using 80-mAs FBP and 8-, 16-, and 32-mAs MBIR.
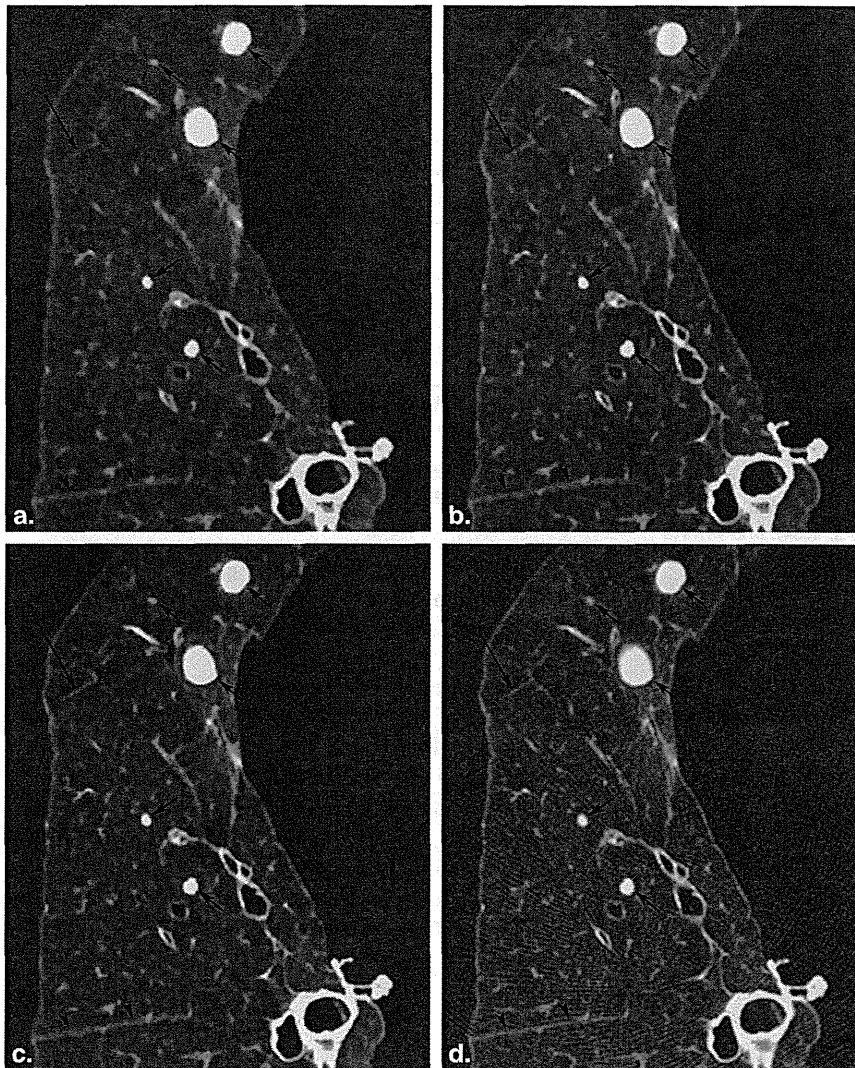
**Figure 3.** Thin-section computed tomographic images of a cadaveric lung with metastases acquired and reconstructed using 8-mAs MBIR **(a)**, 16-mAs MBIR **(b)**, 32-mAs MBIR **(c)**, and 80-mAs FBP **(d)** show similar low level of noise and streak artifacts on the three MBIR images, irrespective of dose. Conspicuity and visibility of peripheral vessels (*long arrow*), interlobar fissure (*arrowheads*), and margins of small and large nodules (*short arrows*) are worse on 8-mAs **(a)**, similar on 16-mAs **(b)**, and better on 32-mAs MBIR **(c)** images as compared to standard-dose FBP **(d)**. FBP, filtered back projection; MBIR, model-based iterative reconstruction.

## DISCUSSION

The principle of ALARA (as low as reasonably achievable) urges radiologists to use the minimum level of radiation needed in imaging examinations to achieve the necessary diagnostic results. Iterative reconstruction algorithms are one of the newer options in the available dose reduction armamentarium that has included restriction of length of coverage, reduced tube voltage, and tube current modulation (11). Of the two iterative reconstruction algorithms evaluated in this study, ASIR, which was introduced earlier, has been more extensively studied (1–8,21–23) and has now largely been implemented into routine clinical practice. In comparison, MBIR, a more mathematically complex reconstruction technique, offers greater potential in dose reduction but at the cost of longer reconstruction times on the order of 45–60 minutes per series (10,11,24). Few studies to date (10–14) have evaluated image quality and diagnostic adequacy of ultra-low-dose MBIR for thin-section chest CT studies.

Our study showed that both ASIR and MBIR can improve lung image quality on ultra-low-dose CT as compared to FBP with MBIR images rated highest. These results are consistent with those of prior clinical studies (10,14) that have reported that when scanning at submillisievert doses, MBIR is superior to ASIR in generating diagnostically acceptable thin-section chest CT images largely because of marked reductions in image noise.

Of the four different iterative reconstructions performed in our study, overall image quality, image noise, and streak artifact were each rated best for MBIR and sequentially decreased with lower blends of ASIR ($ASIR_{90} > ASIR_{60} > ASIR_{30}$). Although a pixilated blotchy appearance has previously been described in association with high-percentage ASIR blends (6,22), this feature was not observed in this study likely related to interval improvements of the ASIR algorithm by the vendor (10). A blotchy appearance however was characteristic of MBIR images, which rendered blinding of
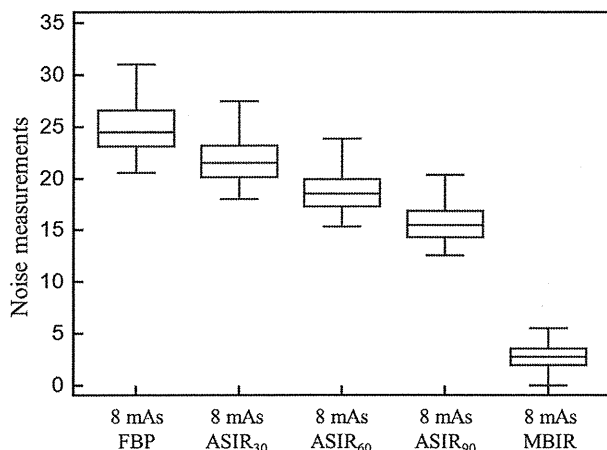
**Figure 4.** Quantitative noise measurements (mean ± standard deviation): 8-mAs FBP (24.7 ± 2.21), 8-mAs $ASIR_{30}$ (21.6 ± 2.01), 8-mAs $ASIR_{60}$ (18.5 ± 1.81), 8-mAs $ASIR_{90}$ (15.5 ± 1.64), and 8-mAs MBIR (2.71 ± 1.10). Significant differences in quantitative noise measurements were found among all groups ($P$ < .001). ASIR, adaptive statistical iterative reconstruction; FBP, filtered back projection; MBIR, model-based iterative reconstruction.



**Figure 5.** Quantitative noise measurements (mean ± standard deviation): 80-mAs FBP (11.99 ± 2.01), 8-mAs MBIR (2.73 ± 1.11), 16-mAs MBIR (2.42 ± 1.10), and 32-mAs MBIR (2.12 ± 1.10). Significant differences in quantitative noise measurements were found among all groups ($P$ < .001). FBP, filtered back projection; MBIR = model-based iterative reconstruction.

observers impossible but did not adversely impact conspicuity or visibility of the CT findings evaluated in this study, namely central and peripheral airways and vessels, interlobar fissures, nodules, GGOs, and thickened interlobular septa. We did, however, observe obscuration of intralobular reticular opacities on MBIR images of one lung specimen with a "crazing paving" pattern because of diffuse alveolar hemorrhage. We postulate that visibility of these fine low-contrast abnormalities may be decreased on the ultra-low-dose MBIR images. Further research on diagnostic adequacy of low-dose MBIR images for broader spectrum of lung abnormalities including those of intrinsic low contrast is required before this technique can be adopted into routine clinical practice.

Although not possible in clinical patients, using this cadaveric lung model, we were able to perform multiple acquisitions to determine the minimum tube current–time product at which image quality of a low-dose MBIR study is comparable to that of a standard-dose FBP study. Of the three tube currents tested, 32-mAs MBIR images were rated highest with statistically significant improvements in conspicuity of each evaluated category of normal and abnormal CT findings, level of image noise, presence of streak artifact, and overall image quality. We found no significant difference in conspicuity of evaluated CT findings (GGOs, nodules, and interlobular septa) between 16-mAs MBIR as compared to 80-mAs FBP despite an 80% reduction in effective dose. At 90% dose reduction, significant decreases in overall image quality and conspicuity of interlobular septal thickening were observed on 8-mAs MBIR images. Thus, MBIR technique enables a submillisievert-dose (0.62 mSv) CT. This effective dose, which is well below the annual exposure from natural sources (3.1 mSv/year), is only 10 times greater than that delivered with two-view radiography (0.06 mSv for standard
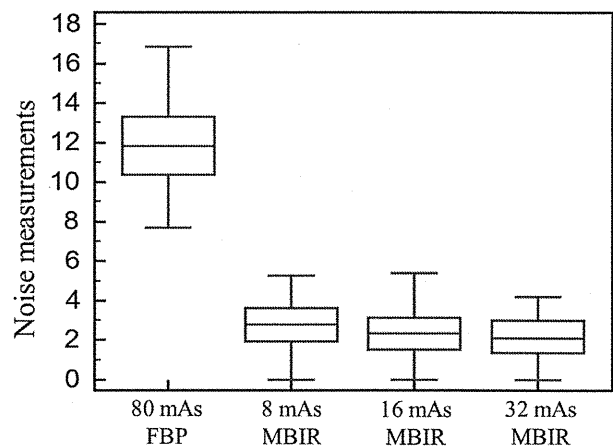
patient), including posteroanterior- and lateral-projection acquisitions (15,25).

Neroladaki et al. (14) have similarly reported limitations in detection of some CT findings on ultra-low-dose MBIR images that were acquired in their study at a radiation exposure (100 kVp, 6 mAs) similar to chest radiography. High-contrast lesions such as solid nodules and architectural distortion were consistently identified by three observers, while interobserver agreement for GGOs and emphysema were fair and poor, respectively.

Detectability of nodules on ultra-low-dose MBIR has been investigated by several groups (11,12,14). Using low-dose (50 mAs) FBP as the gold standard, Yamada et al. (12) report average true-positive fractions of 1.0 and 0.944 for calcified and ≥4 mm noncalcified nodules, respectively on ultra-low-dose (4 mAs) MBIR. Katsura et al. (11) compared 5-mAs MBIR to low-dose $ASIR_{50}$ and found no significant differences in detection of nodules ≥4 mm including nodules with nonsolid components; however, as compared to reference dose $ASIR_{50}$, only an average of 10.5 of 18 pure ground-glass nodules were identified on ultra-low-dose MBIR by the two observers.

Our study was limited by the small number of cases with only three types of abnormal CT findings included for formal evaluation; determination of the diagnostic adequacy of ultra-low-dose MBIR technique will require larger sample sizes with inclusion of a broader spectrum of representative lung CT findings that are encountered in clinical practice. The use of a cadaveric lung model did not allow us to evaluate the influence of a chest wall, body habitus, or motion artifacts on image quality. Moreover, histologic sections of cadaveric lungs should have been used to evaluate the fidelity of the various CT images. Because ASIR and MBIR algorithms are both manufactured by the same company, it is unclear as

to whether the results of our studies are applicable to other iterative reconstruction algorithms. Finally, although the image data sets used in the present study were randomized, perfect blinding to MBIR images might be difficult because it may be relatively easy to discriminate MBIR images with no concept of reconstruction algorithm from ASIR and FBP using a high–spatial-frequency algorithm.

In conclusion, ultra–low–dose thin-section CT images of the lung reconstructed using MBIR are of higher overall image quality with less noise and streak artifact than images reconstructed using ASIR. Even nearly 80% dose reduction under the use of MBIR does not degrade overall image quality.

## REFERENCES

1. Prakash P, Kalra MK, Kambadakone AK, et al. Reducing abdominal CT radiation dose with adaptive statistical iterative reconstruction technique. Invest Radiol 2010; 45:202–210.
2. Singh S, Kalra MK, Hsieh J, et al. Abdominal CT: comparison of adaptive statistical iterative and filtered back projection reconstruction techniques. Radiology 2010; 257:373–383.
3. Honda O, Yanagawa M, Inoue A, et al. Image quality of multiplanar reconstruction of pulmonary CT scans using adaptive statistical iterative reconstruction. Br J Radiol 2011; 84:335–341.
4. Gervaise A, Osemont B, Lecocq S, et al. CT image quality improvement using Adaptive Iterative Dose Reduction with wide-volume acquisition on 320-detector CT. Eur Radiol 2012; 22:295–301.
5. Prakash P, Kalra MK, Ackman JB, et al. Diffuse lung disease: CT of the chest with adaptive statistical iterative reconstruction technique. Radiology 2010; 256:261–269.
6. Singh S, Kalra MK, Gilman MD, et al. Adaptive statistical iterative reconstruction technique for radiation dose reduction in chest CT: a pilot study. Radiology 2011; 259:565–573.
7. Funama Y, Taguchi K, Utsunomiya D, et al. Combination of a low-tube-voltage technique with hybrid iterative reconstruction (iDose) algorithm at coronary computed tomographic angiography. J Comput Assist Tomogr 2011; 35:480–485.
8. Moscariello A, Takx RA, Schoepf UJ, et al. Coronary CT angiography: image quality, diagnostic accuracy, and potential for radiation dose reduction using a novel iterative image reconstruction technique-comparison with traditional filtered back projection. Eur Radiol 2011; 21:2130–2138.
9. Thibault JB, Sauer KD, Bouman CA, et al. A three-dimensional statistical approach to improved image quality for multislice helical CT. Med Phys 2007; 34:4526–4544.
10. Katsura M, Matsuda I, Akahane M, et al. Model-based iterative reconstruction technique for radiation dose reduction in chest CT: comparison with

the adaptive statistical iterative reconstruction technique. Eur Radiol 2012; 22:1613–1623.
11. Katsura M, Matsuda I, Akahane M, et al. Model-based iterative reconstruction technique for ultralow-dose chest CT: comparison of pulmonary nodule detectability with the adaptive statistical iterative reconstruction technique. Invest Radiol 2013; 48:206–212.
12. Yamada Y, Jinzaki M, Tanami Y, et al. Model-based iterative reconstruction technique for ultralow-dose computed tomography of the lung: a pilot study. Invest Radiol 2012; 47:482–489.
13. Vardhanabhuti V, Loader RJ, Mitchell GR, et al. Image quality assessment of standard- and low-dose chest CT using filtered back projection, adaptive statistical iterative reconstruction, and novel model-based iterative reconstruction algorithms. AJR Am J Roentgenol 2013; 200:545–552.
14. Neroladaki A, Botsikas D, Boudabbous S, et al. Computed tomography of the chest with model-based iterative reconstruction using a radiation exposure similar to chest X-ray examination: preliminary observations. Eur Radiol 2013; 23:360–366.
15. McCollough CH, Chen GH, Kalender W, et al. Achieving routine submillisievert CT scanning: report from the summit on management of radiation dose in CT. Radiology 2012; 264:567–580.
16. Markarian B, Dailey ET. Preparation of inflated lung specimens. In: Groskin SA, ed. Heitzman's The lung: radiologic-pathologic correlations. 3rd ed. St. Louis: Mosby, 1993; 4–12.
17. Aberle DR, Berg CD, Black WC, et al. The National Lung Screening Trial: overview and study design. Radiology 2011; 258:243–253.
18. Boehm T, Willmann JK, Hilfiker PR, et al. Thin-section CT of the lung: dose electrocardiographic triggering influence diagnosis? Radiology 2003; 229(2):483–491.
19. Goldman LW. Principles of CT: radiation dose and image quality. J Nucl Med Technol 2007; 35:213–225.
20. American Association of Physicists in Medicine. The measurement, reporting, and management of radiation dose in CT; 2008. Available at: http://www.aapm.org/pubs/reports/rpt_96.pdf. Accessed January 15, 2012.
21. Marin D, Nelson RC, Schindera ST, et al. Low-tube-voltage, high-tube-current multidetector abdominal CT: improved image quality and decreased radiation dose with adaptive statistical iterative reconstruction algorithm—initial clinical experience. Radiology 2010; 254:145–153.
22. Yanagawa M, Honda O, Yoshida S, et al. Adaptive statistical iterative reconstruction technique for pulmonary CT: image quality of the cadaveric lung on standard- and reduced-dose CT. Acad Radiol 2010; 17: 1259–1266.
23. Hara AK, Paden RG, Silva AC, et al. Iterative reconstruction technique for reducing body radiation dose at CT: feasibility study. AJR Am J Roentgenol 2009; 193:764–771.
24. Yu Z, Thibault JB, Bouman CA, et al. Fast model-based X-ray CT reconstruction using spatially nonhomogeneous ICD optimization. IEEE Trans Image Process 2011; 20:161–175.
25. Wall BF, Hart D. Revised radiation doses for typical X-ray examinations. Report on a recent review of doses to patients from medical X-ray examinations in the UK by NRPB. National Radiological Protection Board. Br J Radiol 1997; 70:437–439.

# Prognostic Importance of Volumetric Measurements in Stage I Lung Adenocarcinoma[1]

Masahiro Yanagawa, MD, PhD
Yuko Tanaka, MD
Ann N. Leung, MD
Eiichi Morii, MD, PhD
Masahiko Kusumoto, MD, PhD
Shunichi Watanabe, MD, PhD
Hirokazu Watanabe, MD, PhD
Masayoshi Inoue, MD, PhD
Meinoshin Okumura, MD, PhD
Tomoko Gyobu, MD
Ken Ueda, MD
Osamu Honda, MD, PhD
Hiromitsu Sumikawa, MD, PhD
Takeshi Johkoh, MD, PhD
Noriyuki Tomiyama, MD, PhD

**Purpose:** To perform volumetric analysis of stage I lung adenocarcinomas by using an automated computer program and to determine value of volumetric computed tomographic (CT) measurements associated with prognostic factors and outcome.

**Materials and Methods:-** Consecutive patients ($n$ = 145) with stage I lung adenocarcinoma who underwent surgery after preoperative chest CT were enrolled. By using volumetric automated computer-assisted analytic program, nodules were classified into three subgroups: pure ground glass, part solid, or solid. Total tumor volume, solid tumor volume, and percentage of solid volume of each cancer were calculated after eliminating vessel components. One radiologist measured the longest diameter of the solid tumor component and of total tumor with their ratio, which was defined as solid proportion. The value of these quantitative data by examining associations with pathologic prognostic factors and outcome measures (disease-free survival and overall survival) were analyzed with logistic regression and Cox proportional hazards regression models, respectively. Significant parameters identified at univariate analysis were included in the multiple analyses.

**Results:** All 22 recurrences occurred in patients with nodules classified as part solid or solid. Multiple logistic regression analysis revealed that percentage of solid volume of 63% or greater was an independent indicator associated with pleural invasion ($P$ = .01). Multiple Cox proportional hazards regression analysis revealed that percentage of solid volume of 63% or greater was a significant indicator of lower disease-free survival (hazard ratio, 18.45 [95% confidence interval: 4.34, 78.49]; $P$ < .001). Both solid tumor volume of 1.5 cm$^3$ or greater and percentage of solid volume of 63% or greater were significant indicators of decreased overall survival (hazard ratio, 5.92 and 9.60, respectively [95% confidence interval: 1.17, 30.33 and 1.17, 78.91, respectively]; $P$ = .034 and .036, respectively).

**Conclusion:** Two volumetric measurements (solid volume, ≥1.5 cm$^3$; percentage of solid volume, ≥63%) were found to be independent indicators associated with increased likelihood of recurrence and/or death in patients with stage I adenocarcinoma.

© RSNA, 2014

denocarcinoma is the most common subtype of lung cancer. In 2011, a new classification of adenocarcinoma (1) was developed to standardize diagnostic criteria and terminology applied to the wide spectrum of entities encompassed in this histologic subtype, which can range from indolent to lethal tumors. Results from several studies (2–5) have shown by using computed tomographic (CT) imaging that morphologic structure of adenocarcinoma can be predictive of tumor grade and patient prognosis. As emphasized in the recently published recommendations for subsolid nodules from the Fleischner Society (6), measurement of solid components and determination of the relative percentages of solid versus ground-glass portions of subsolid nodules are important because an increase in the extent of a solid component is associated with a higher likelihood of an invasive tumor. However, integration of this type of prognostic CT data into clinical management algorithms for adenocarcinoma has been relatively hindered by the lack of standardized methods for tumor characterization and measurement, particularly in the setting of part-solid nodules.

Volumetric measurement of nodules is a promising technique that has been shown (7–11) to be both accurate and precise for the quantification of small solid nodules. However, volumetric assessment of subsolid nodules is more challenging because of difficulties in segmentation and accurate

delineation between a tumor's ground-glass margins and the adjacent normal parenchyma. By using manual measurements, de Hoop et al (12) compared diameter, volume, and mass (volume × CT value) of 52 ground-glass nodules (GGNs) that were followed as part of a lung cancer screening trial; among the three measures, they found that mass of GGN was subject to less variability and allowed earliest detection of growth in malignant nodules. Ko et al (11) reported similar growth-related results in five solid and three subsolid malignant nodules that were detected earlier with volumetric measurements obtained by using a semiautomated computer algorithm than with radiologic criteria used in current practice.

We hypothesized that volumetric measurement of solid and nonsolid components of early-stage adenocarcinoma seen by using CT imaging can provide prognostic information. The purpose of our study was to perform volumetric analysis of stage I lung adenocarcinomas by using an automated computer program and to determine the value of volumetric CT measurements associated with prognostic factors and patient outcome.

## Materials and Methods

### Patients

We obtained approval from our internal institutional review board; informed consent was waived for retrospective review of patient records and images. The study population consisted of 145 consecutive patients (68 men and 77 women; mean age, 63.6 years ± 9.6 [standard deviation]; range, 31–82 years) who had undergone lobectomy ($n = 104$) or segmentectomy ($n = 41$) for pathologic stage I adenocarcinoma

at our hospital from April 1999 to April 2006 and had a preoperative thin-section chest CT study available for review. All patients were node-negative based on fluorine 18 fluorodeoxyglucose (FDG) positron emission tomographic (PET) staging study. Hilar and mediastinal lymph node resections were performed in 104 patients with lobectomy, and hilar lymph nodal sampling was performed in 41 patients with segmentectomy at the time of tumor resection. Individuals who had history of adenocarcinoma of the lung or other organs or who had received induction chemotherapy before surgery were excluded from the study.

After hospital discharge, all patients were evaluated at 3-month intervals. The evaluation included a physical examination, chest x-ray, and blood tests (including tumor markers). Additional thoracoabdominal CT scans were generally obtained at 6-month intervals. Recurrence was confirmed at CT and, if necessary, FDG PET imaging. The median follow-up period of all 145 patients after surgery was 6.2 years (range, 0.86–12.63 years). Complete follow-up information until death or January 2013 was available for all patients. During the follow-up period, 22 patients experienced disease recurrence with seven associated cancer-related deaths.

### Advances in Knowledge

- Automated volumetric analysis of stage I adenocarcinoma allowed quantification of CT features associated with patient outcome.
- Radiologist and software classification of nodules into subsolid and solid subtypes showed excellent agreement ($\kappa = 0.81$).
- Volumetric measurements of tumor solid component and percentage of solid volume were associated with recurrence and/or death, whereas measurement of total tumor volume was not.

### Implication for Patient Care

- Automated volumetric analysis of early-stage adenocarcinomas can be associated with prognosis and may be helpful in determining appropriate treatment of patients with subsolid nodules.

## Scanning Protocols

Chest CT scans were acquired by using a four–detector row CT scanner (Light-Speed QXi; GE Healthcare, Milwaukee, Wis) and an eight–detector row CT scanner (LightSpeed Ultra; GE Healthcare). Acquisition parameters were as follows: collimation, 0.625 mm or 1.25 mm; pitch, 0.625–1.5; rotation time, 0.4–0.8 seconds per rotation; exposure parameters, 120 kV and 200 mA; field of view, 200 mm. All image data were reconstructed with a high spatial frequency algorithm at contiguous section thicknesses of 0.625 mm or 1.25 mm.

## Visual Analysis

CT scans were displayed on a monitor at lung window settings (level, −700 HU; width, 1200 HU). Two independent chest radiologists (G.T. and H.S., with 9 and 13 years of experience, respectively) visually classified tumors into three subgroups: pure GGN, part-solid GGN, and solid. GGN was defined as an area that exhibited a slight, homogeneous increase in density, which did not obscure underlying vascular markings. Solid was defined as an area of increased opacity that completely obscured underlying vascular markings. The two radiologists designated the distribution of each nodule as peripheral (outer one-third of lung, but not in contact with pleura), middle (inner two-thirds of lung), or juxtapleural (in contact with pleura). Final evaluations were decided by a consensus panel, which consisted of the same two radiologists and an adjudicator (O.H., with 21 years of experience in chest radiologic imaging), as needed. By using electronic calipers, one chest radiologist (M.Y., with 12 years of experience) measured the longest diameter of the solid component and of total tumor; solid proportion was defined as the ratio of the longest diameter of the solid component divided by the longest diameter of total tumor multiplied by 100%.

## Computer Analysis

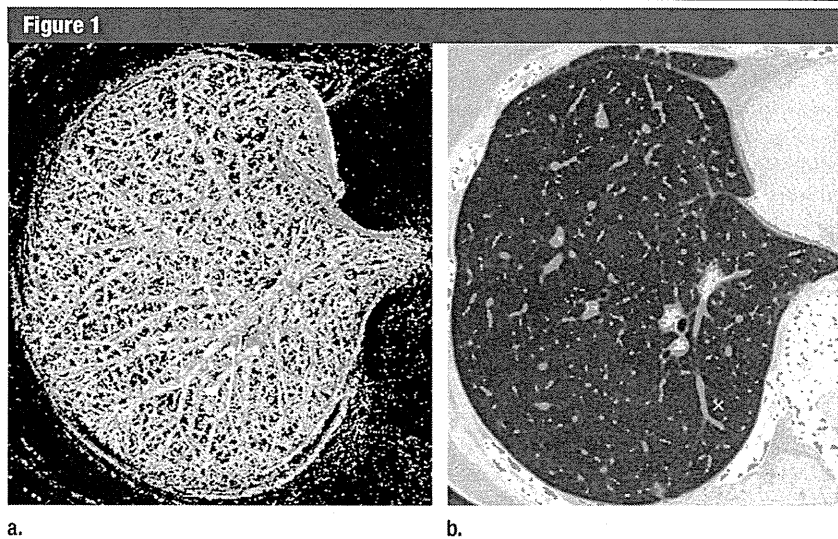We developed our software by using commercial software (Microsoft Visual C++ 6.0; Microsoft, Redmond, Wash) on a commercially available personal computer. Incorporated in our software is a previously described (13) three-dimensional line filter that enabled the enhancement of curvilinear structures, such as vessels, in three-dimensional medical images on the basis of a combination of the eigenvalues of the three-dimensional Hessian matrix. Multiscale integration is formulated by taking the maximum among single scale filter responses, and its characteristics are examined to derive criteria for the selection of parameters in the formulation. The resultant multiscale line-filtered images provide improved segmentation and visualization of curvilinear structures. This three-dimensional line filter was used as the first step to eliminate vessels on the CT images (Fig 1). Quantitative analysis was then performed by one observer (M.Y., 12 years of experience in chest radiology) who was required to place an over-inclusive region of interest around each nodule after selecting a tumor center point (ie, a seed point) (Fig 2). The threshold value on CT between a tumor and surrounding normal lung parenchyma was automatically determined by applying CT density profile curves, one-dimensional quantitative CT values across the nodule, through the seed point at 10° intervals on each axial section



**Figure 1:** Images show extraction of vessels by using a multiscale three-dimensional line filter. **(a)** Volume rendering image of all vessels identified by the three-dimensional line filter. **(b)** Green areas in right lung correspond to extracted vessels.

(14) (Fig 3a). A CT value that corresponded to full width at half maximum (FWHM) was measured from each profile curve, and the mean FWHM from the 36 density profiles was used as threshold value (Fig 3b). FWHM is a mathematically well-defined parameter used to describe a measurement of the width of an object in imaging when that object does not have sharp edges. The width of the CT density profile curve is often decided by the FWHM (15,16). Following this approach, we used the CT value that corresponded to mean FWHM as an objective, standardized method to determine the threshold CT value between the tumor and surrounding normal lung parenchyma.

The tumor was also segmented by using a three-dimensional region-growing algorithm (17) that, after placement of an initial seed point, added in neighboring pixels with attenuation values above defined threshold value that did not contain vessels. The volume of the tumor was calculated as follows: (number of voxels within segmented region) × unit volume. Unit volume was defined as the product of x-, y-, and z-axes in a raw image.

On the basis of a previously reported threshold selection and nodule classification method (18), we used
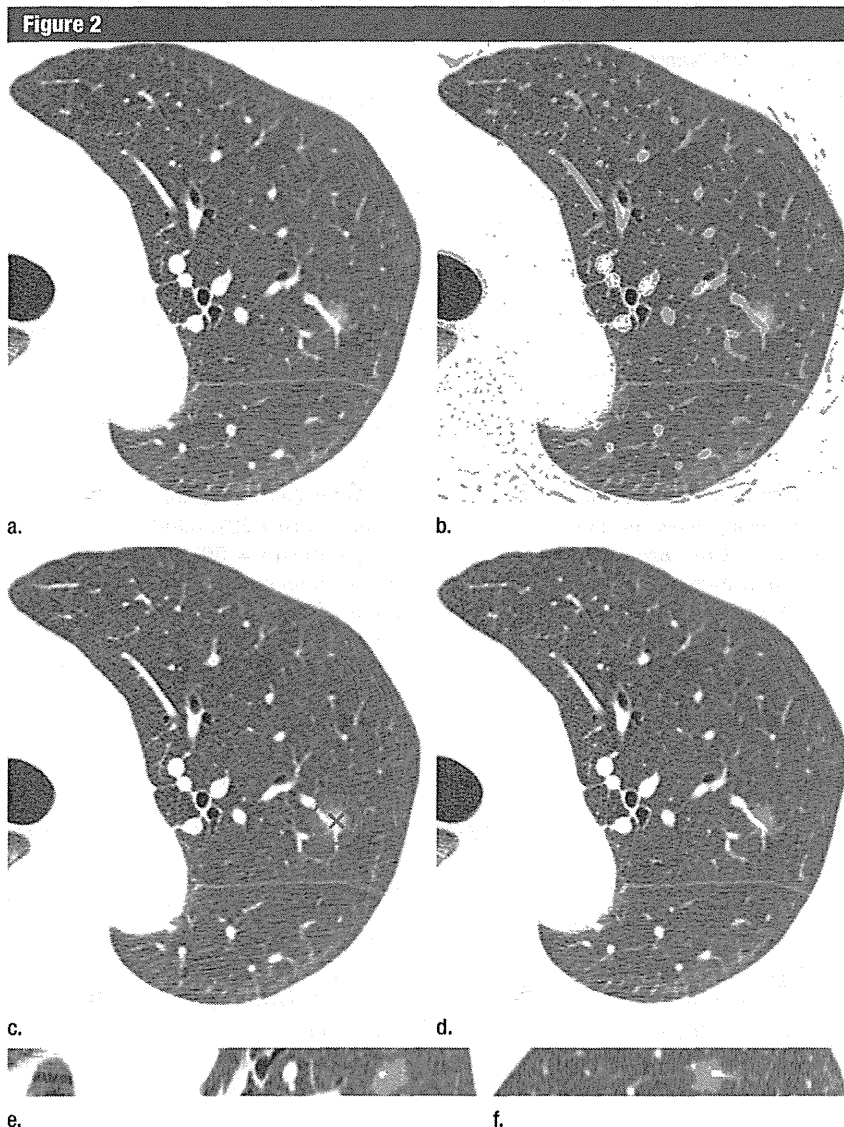
**Figure 2:** Images show sequential steps in volumetric analysis of a pure GGN in a 57-year-old woman. **(a)** Thin-section CT image shows a pulmonary vein traversing an 8.1-mm GGN in the left upper lobe. **(b)** Three-dimensional line filter identifies and extracts vessels (green areas). **(c)** An over-inclusive region of interest is drawn manually around the nodule in red. **(d)** Axial image, **(e)** coronal image, and **(f)** sagittal image of GGN. Nodule is automatically segmented (shown as highlighted green area) with calculation of GGN and solid components. Total volume, solid volume, and percentage of solid volume for this nodule are 0.14 cm³, 0.00 cm³, and 0.00%, respectively.



**Figure 3:** Threshold CT value between a tumor and surrounding normal lung parenchyma in a 60-year-old woman. **(a)** CT density profile curves are drawn through center of nodule at 10° intervals. **(b)** A representative profile curve shows CT value at FWHM is −545 HU (arrow). The mean CT value derived from all 36 profile curves on each axial section is used as the threshold CT value.

attenuation greater than −291 HU]) (18). Before beginning this study, we performed computer-assisted analysis of 10 nodules that were not included in this study that by qualitative evaluation consisted of pure ground-glass attenuation. In these 10 cases, percentage of solid volume ranged from 0% to 1.9% (mean, 0.8% ± 1.1% [standard deviation]); therefore, percentage of solid volume in the GGN subgroup was defined as less than 2%.

**Pathologic Analysis**

The presence of lymphatic, vascular, and pleural invasion was evaluated by two pathologists. Final evaluation was decided in consensus. Immunostaining methods by using D2-40 (Covance, San Diego, Calif), a lymphatic-specific monoclonal antibody, and CD31 (Dako, Glostrup, Denmark), an endothelial antigen, were performed to optimize identification of lymphatic and vascular channels, respectively (19,20).

−291 HU as the threshold CT value between ground glass and solid. By using this value, each voxel of ground glass and solid included in a segmented tumor was automatically determined; total tumor volume, solid volume, and percentage of solid volume (solid volume/tumor volume × 100%) were calculated; and the nodule was classified into three subgroups (pure GGN [>98% of tumor with attenuation of −291 HU or less], part-solid GGN [2%–71.5% of tumor with attenuation greater than −291 HU], and solid [>71.5% of tumor with
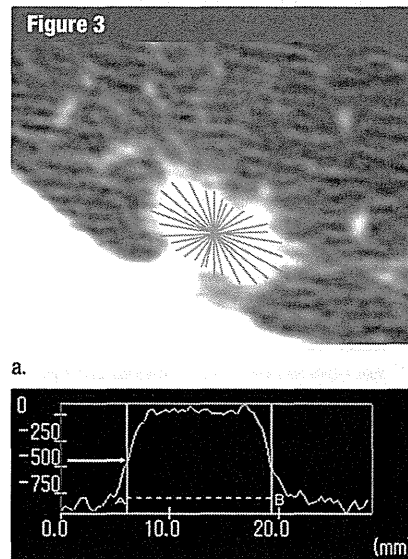
## Table 1

### Quantitative Measurements in 145 Patients with Stage I Adenocarcinoma

| Parameter | All Patients | Patients with Pure GGN | Patients with Part-Solid GGN | Patients with Solid Tumor |
|---|---|---|---|---|
| Visual analysis | | | | |
| Longest diameter of tumor (mm) | 15.7 ± 4.8 (7.0–31.0) | 11.2 ± 2.7 (7.0–14.9) | 15.9 ± 4.6 (7.2–31.0) | 16.9 ± 5.1 (7.0–31.0) |
| Longest diameter of solid component (mm) | 9.6 ± 7.0 (0.0–31.0) | 0.0 ± 0.0 (0.0–0.0) | 7.5 ± 4.7 (1.0–21.0) | 16.9 ± 5.1 (7.0–31.0) |
| Solid proportion (%) | 58.3 ± 37.1 (0.0–100.0) | 0.0 ± 0.0 (0.0–0.0) | 47.2 ± 26.5 (11.4–95.0) | 100.0 ± 0.0 (100.0–100.0) |
| Computer analysis | | | | |
| Tumor volume (cm$^3$) | 2.46 ± 2.87 (0.03–16.97) | 0.64 ± 0.54 (0.03–1.62) | 1.92 ± 2.23 (0.05–15.60) | 4.01 ± 3.58 (0.45–16.97) |
| Solid volume (cm$^3$) | 1.47 ± 2.18 (0.00–14.28) | 0.00 ± 0.02 (0.00–0.12) | 0.75 ± 0.82 (0.003–4.09) | 3.22 ± 3.00 (0.35–14.28) |
| Solid volume (%) | 49.1 ± 28.2 (0.00–90.40) | 0.21 ± 0.5 (0.00–1.90) | 40.9 ± 19.9 (6.30–71.50) | 78.7 ± 5.0 (71.60–90.40) |

Note.—Data are mean ± standard deviation. Data in parentheses are range. For group classification, there were 145 patients total, 15 with pure GGN, 83 with part-solid GGN, and 47 with solid tumor. For visual analysis, there were 145 patients total, 15 with pure GGN, 86 with part-solid GGN, and 44 with solid tumor.

## Statistical Analysis

We evaluated the value of eight features of CT (visual classification, software classification, longest diameter of solid component, longest diameter of total tumor, solid proportion, total tumor volume, solid volume, and percentage of solid volume) to examine associations with three prognostic factors (lymphatic invasion, vascular invasion, and pleural invasion) and two outcome measures (overall survival and disease-free survival). All statistical analyses were performed by using commercially available software (MedCalc version 8.0.0.1; Frank Schoonjans, Mariakerke, Belgium). Agreement between visual and software classification of nodule subgroups was evaluated by using the κ statistic, and it was classified as poor (κ = 0.00–0.20), fair (κ = 0.21–0.40), moderate (κ = 0.41–0.60), good (κ = 0.61–0.80), or excellent (κ = 0.81–1.00) (21). For each CT feature, the cutoff value that yielded the largest difference in numbers of patients with and without recurrence and death was determined by using the empirical receiver operating characteristic method. Receiver operating characteristic analyses were all univariate. The optimal thresholds were determined for each variable separately. Subsequently, associations between prognostic factors and each binary group designated by the cutoff value for the eight CT features were evaluated by using univariate logistic regression analysis. Similarly, associations

between outcome measures and each binary group were evaluated by using univariate Cox proportional hazards regression analysis. Significant parameters identified by univariate analysis were included in the multiple logistic regression and Cox proportional hazards regression models (stepwise method; P value of .05 or less was used for entry into the model and P value greater than .1 was selected for removal), respectively. The 123 patients (85.0%) with no observed failure events in the present study were considered censored for the two outcome measures in the Cox proportional hazards regression model. Survival curves were generated by the Kaplan-Meier method, with comparisons performed by using the log-rank test. A P value of less than .05 indicated statistical significance.

## Results

### Visual and Computer Analyses

Results of all 145 patients are summarized in Table 1. Classification of nodules (per two radiologists) into pure GGN, part-solid GGN, and solid subtypes showed excellent agreement (κ = 0.90). There was excellent agreement (κ = 0.81) between visual and computer classification of nodule subgroups with disagreements on only five nodules.

Distribution of pure GGN was peripheral (n = 12), middle (n = 2), and juxtapleural (n = 1); distribution of

part-solid GGN and solid nodules was peripheral (n = 72), middle (n = 8), and juxtapleural (n = 50). Mean measured longest diameter of solid component and total tumor were 9.6 mm ± 7.0 (range, 0–31.0 mm) and 15.7 mm ± 4.8 (range, 7.0–31.0 mm), respectively. Calculated solid proportion of nodules was 58.3%–37.1% (range, 0%–100%). Total tumor volume, solid volume, and percentage solid volume were 2.46 cm$^3$ ± 2.87 (range, 0.033–16.97 cm$^3$), 1.47 cm$^3$ ± 2.18 (range, 0–14.28 cm$^3$), and 49.1% ± 28.2 (range, 0%–90.4%), respectively.

### Pathologic Analysis

There were identified lymphatic invasion in 17 cases, pleural invasion in 13 cases, and no cases of vascular invasion. There were 118 patients staged as pT1a, 14 patients staged as pT1b, and 13 patients staged as pT2. No patients were found to have lymph node metastases. According to pathologic analysis, there were 132 patients staged as Ia and 13 patients staged as Ib.

### Relationship with Prognostic Factors

On the basis of receiver operating characteristic analysis, both visually and computer-classified subgroups were re-sorted into pure GGN and solid (part-solid GGN and solid) divisions. Cutoff values for the six CT features were as follows: longest diameter of solid component, 9.9 mm; longest tumor diameter, 18 mm; solid proportion, 78%; total tumor volume,

## Table 2

### Relationship of CT Features with Prognostic Factors

| Logistic Regression Analysis | Lymphatic Invasion ($n = 145$) | | | Pleural Invasion ($n = 51$) | | |
|---|---|---|---|---|---|---|
| | No. of Tumors | Odds Ratio | P Value | No. of Tumors | Odds Ratio | P Value |
| Univariate analysis | | | | | | |
| Visual classification | | | | | | |
| Pure GGN | 15 | 1.96 (0.24, 15.97) | .49 | 1 | ND* | ND* |
| Solid | 130 | ... | ... | 50 | ND* | ND* |
| Software classification | | | | | | |
| Pure GGN | 15 | 1.96 (0.24, 15.97) | .49 | 0 | ND* | ND* |
| Solid | 130 | ... | ... | 51 | ND* | ND* |
| Longest diameter of tumor | | | | | | |
| <18 mm | 94 | 1.01 (0.35, 2.90) | .99 | 27 | 0.95 (0.27, 3.37) | .94 |
| ≥18 mm | 51 | ... | ... | 24 | ... | ... |
| Longest diameter of solid component | | | | | | |
| <9.9 mm | 81 | 2.17 (0.67, 6.99) | .19 | 21 | 3.00 (0.71, 12.65) | .13 |
| ≥9.9 mm | 64 | ... | ... | 30 | ... | ... |
| Solid proportion | | | | | | |
| <78% | 90 | 2.04 (0.65, 6.43) | .22 | 24 | 4.12 (0.98, 17.38) | .05 |
| ≥78% | 55 | ... | ... | 27 | ... | ... |
| Total tumor volume | | | | | | |
| <1.9 cm³ | 84 | 0.96 (0.34, 2.68) | .94 | 21 | 1.16 (0.32, 4.23) | .81 |
| ≥1.9 cm³ | 61 | ... | ... | 30 | ... | ... |
| Solid volume | | | | | | |
| <1.5 cm³ | 101 | 1.29 (0.45, 3.75) | .64 | 26 | 1.30 (0.37, 4.58) | .69 |
| ≥1.5 cm³ | 44 | ... | ... | 25 | ... | ... |
| Percentage of solid volume | | | | | | |
| <63% | 88 | 2.46 (0.88, 6.90) | .08 | 23 | 6.03 (1.58, 22.98) | .01 |
| ≥63% | 57 | ... | ... | 28 | ... | ... |
| Multiple analysis (by stepwise method) | | | | | | |
| Percentage of solid volume | | | | | | |
| <63% | 88 | ND | ND | 23 | 6.03 (1.58, 22.98) | .01 |
| ≥63% | 57 | ND | ND | 28 | ... | ... |

Note.—Data in parentheses are 95% confidence intervals. P values less than .05 indicated statistical significance. ND = no data.
* Statistical analysis for association with pleural invasion could not be performed because of a small number of juxtapleural nodules in GGN division.

---

1.9 cm³; solid volume, 1.5 cm³; and solid volume, 63%.

Results for association of eight CT features with two prognostic factors are summarized in Table 2. Statistical analysis was performed to examine associations with lymphatic invasion in 145 cases and pleural invasion in 51 cases; none of the resected tumors were found by using pathologic examination to have vascular invasion. Statistical analysis for examining the association with pleural invasion was performed only for those tumors that were juxtapleural in location. None of the eight CT features were found to be of use in examination of presence of lymphatic invasion. Univariate and multiple logistic regression analyses revealed that percentage of solid volume of 63% or greater was of significant use in examination of presence of pleural invasion (odds ratio, 6.03 [95% confidence interval: 1.58, 22.98]; P = .01).

### Relationship with Recurrence and Survival

During a 7-year follow-up period, 22 patients experienced disease recurrence, and there were seven associated cancer-related deaths. All cases of recurrence and death occurred in patients with tumors classified as part-solid GGN ($n = 6$) or solid ($n = 16$); none occurred in patients with tumors classified as GGN.

Results for relationship of eight CT features with disease-free survival and overall survival are summarized in Table 3. Multiple analyses showed that percentage of solid volume of 63% or greater was a significant indicator for lower disease-free survival ($P < .001$). Both univariate and multiple analyses showed that solid volume of 1.5 cm³ or greater and three-dimensional percentage of solid of 63% or greater were significant ($P < .05$) indicators for lower overall survival. Figures 4 and 5 show the lower disease-free and

**Table 3**

### Association of CT Features with Survival

| Cox Proportional Hazards Regression Analysis | No. of Tumors | Disease-free Survival | | Overall Survival | |
|---|---|---|---|---|---|
| | | Hazard Ratio | P Value | Hazard Ratio | P Value |
| Univariate analysis | | | | | |
| Visual classification | | | | | |
| Pure GGN | 15 | 310 644 (0.00, 3.48 × 10$^{198}$) | .097 | 113 504 (0.00, 5.23 × 10$^{198}$) | .375 |
| Solid | 130 | ... | ... | ... | ... |
| Software classification | | | | | |
| Pure GGN | 15 | 310 644 (0.00, 3.48 × 10$^{198}$) | .097 | 113 504 (0.00, 5.23 × 10$^{198}$) | .375 |
| Solid | 130 | ... | ... | ... | ... |
| Longest diameter of tumor | | | | | |
| <18 mm | 94 | 2.89 (1.19, 6.98) | .012 | 2.65 (0.57, 12.22) | .207 |
| ≥18 mm | 51 | ... | ... | ... | ... |
| Longest diameter of solid component | | | | | |
| <9.9 mm | 81 | 9.23 (2.74, 31.02) | <.001 | 7.93 (0.96, 65.19) | .055 |
| ≥9.9 mm | 64 | ... | ... | ... | ... |
| Solid proportion | | | | | |
| <78% | 90 | 8.12 (2.76, 23.87) | <.001 | 4.32 (0.84, 22.08) | .080 |
| ≥78% | 55 | ... | ... | ... | ... |
| Total tumor volume | | | | | |
| <1.9 cm$^3$ | 84 | 4.57 (1.96, 11.43) | .001 | 3.81 (0.84, 12.31) | .086 |
| ≥1.9 cm$^3$ | 61 | ... | ... | ... | ... |
| Solid volume | | | | | |
| <1.5 cm$^3$ | 101 | 7.17 (2.79, 18.35) | <.001 | 5.90 (1.17, 29.80) | .016 |
| ≥1.5 cm$^3$ | 44 | ... | ... | ... | ... |
| Percentage of solid volume | | | | | |
| <63% | 88 | 8.18 (2.80, 18.35) | <.001 | 9.58 (2.09, 43.91) | .01 |
| ≥63% | 57 | ... | ... | ... | ... |
| Multiple analysis (by stepwise method) | | | | | |
| Solid volume | | | | | |
| <1.5 cm$^3$ | 101 | ... | ... | 5.92 (1.17, 30.33) | .034 |
| ≥1.5 cm$^3$ | 44 | ... | ... | ... | ... |
| Percentage of solid volume | | | | | |
| <63% | 88 | 18.45 (4.34, 78.49) | <.001 | 9.60 (1.17, 78.91) | .036 |
| ≥63% | 57 | ... | ... | ... | ... |

Note.—Data in parentheses are 95% confidence intervals. P values less than .05 indicate statistical significance.

overall survival for patients with solid volume of 1.5 cm$^3$ or greater (7-year disease-free survival and overall survival rates, 58.6% and 85.1%, respectively) and percentage of solid volume of 63% or greater (7-year disease-free survival and overall survival rates, 60.1% and 86.3%, respectively) compared with patients with solid volume less than 1.5 cm$^3$ (7-year disease-free survival and overall survival rates, 92.4% and 98.0%, respectively; $P \leq$ .015) and percentage of solid volume of less than 63% (7-year disease-free survival and overall survival rates,

96.3% and 98.9%, respectively; $P \leq$ .01).

Table 4 shows quantitative measurements, types of resection performed, and sites of recurrence in 22 patients with recurrence and death. Of the eight smallest tumors that were less than 15.5 mm in longest diameter, six tumors (75%) had solid volume of less than 1.5 cm$^3$ and one (13%) had percent solid volume of less than 63%. A 27-mm part-solid tumor that resulted in patient death had multiple foci of solid components with measured solid volume of 2.77 cm$^3$ and percentage of

solid volume of 29.8% (Fig 6). Ten patients with recurrent disease presented with a solitary lung metastasis that (based upon either biopsy or resection findings) was confirmed to be adenocarcinoma. Only one nodule recurred in the primary tumor lobe of a patient who had undergone segmentectomy; the remaining nine nodules recurred in a nonprimary tumor lobe and were clinically judged to more likely represent metastatic disease than metachronous primaries based on temporal evolution as documented on postoperative surveillance imaging studies.
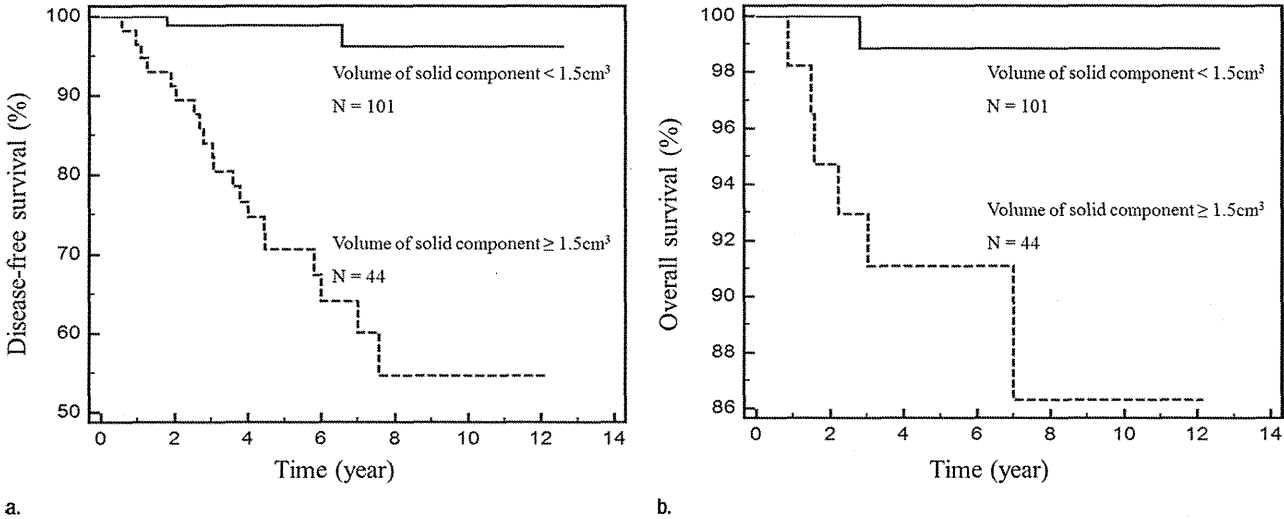
**Figure 4:**    Kaplan-Meier survival curves show that patients with solid tumor volume of 1.5 cm$^3$ or greater had a significantly lower probability of **(a)** disease-free ($P$ < .001) and **(b)** overall survival ($P$ = .015) than patients with solid tumor volume less than 1.5 cm$^3$.
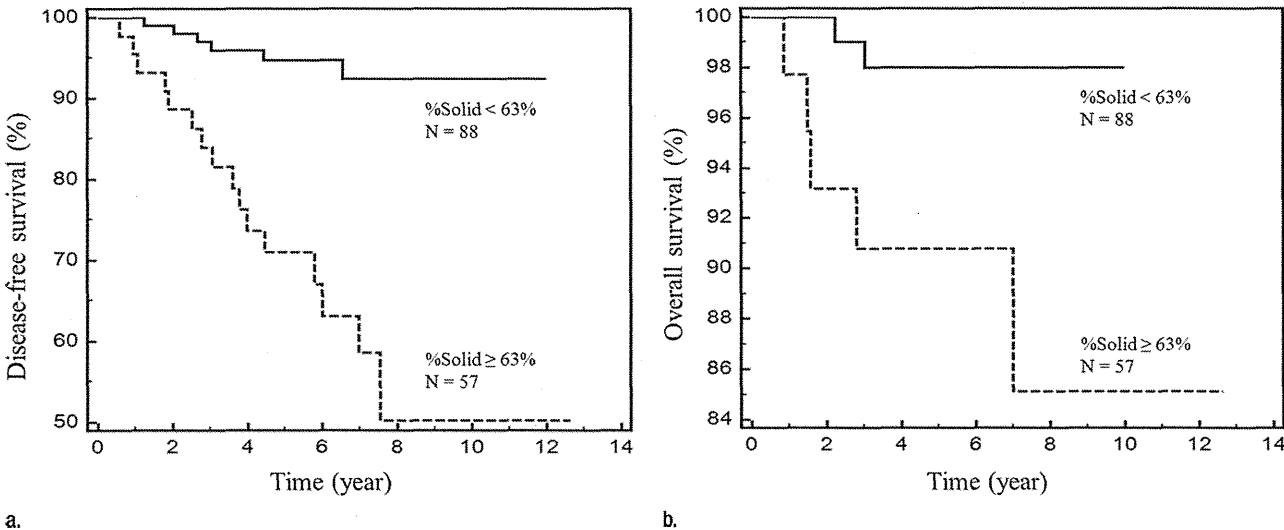


**Figure 5:**    Kaplan-Meier survival curves show that patients with percentage of solid tumor volume of 63% or greater had a significantly lower probability of **(a)** disease-free ($P$ < .001) and **(b)** overall survival ($P$ = .010) than patients with percentage of solid tumor volume of less than 63%.

## Discussion

Clinical algorithms for optimal management of adenocarcinomas that manifest as subsolid nodules by using CT imaging remain an area of active controversy. In two guidelines recently published by the Fleischner Society (6) and American College of Chest Physicians (22), there was disagreement as to whether total diameter or diameter of only the solid component of a part-solid GGN should be used as the predictive feature that determines triage into alternate management pathways. A more fundamental controversy is whether solid tumor components visualized by using CT imaging should be measured on mediastinal or lung windows (23).

In our study, we used a volumetric automated computer-assisted method to analyze early-stage adenocarcinomas and link the analytic output, including volumetric measurements, to prognostic

## Table 4

### Quantitative Measurements in 22 Patients with Recurrence and Death

| Case No. | Longest Diameter of Tumor (mm) | Longest Diameter of Solid Component (mm) | Solid Proportion (%) | Total Volume (cm³) | Solid Volume (cm³) | Percentage of Solid Volume (%) | Type of Surgery | Site of Recurrence |
|---|---|---|---|---|---|---|---|---|
| Recurrence | | | | | | | | |
| 1 | 13.7 | 4.8 | 35.04 | 1.26 | 0.48* | 38.1† | Seg (LLL) | Lung (RUL) |
| 2 | 19 | 16.7 | 87.89 | 2.88 | 2.04 | 70.8 | L (LUL) | Lung (LLL) |
| 3 | 21.4 | 18.1 | 84.58 | 4.5 | 2.87 | 63.8 | Seg (LUL) | Lung (LUL) |
| 4 | 10 | 10 | 100 | 0.45 | 0.34* | 75.6 | Seg (RLL) | Lung (multiple) |
| 5 | 12 | 12 | 100 | 0.82 | 0.67* | 81.7 | L (RML) | Lung (RUL) |
| 6 | 12 | 12 | 100 | 0.9 | 0.62* | 68.9 | Seg (LUL) | Lung (RML) |
| 7 | 13.3 | 13.3 | 100 | 2.38 | 1.92 | 80.7 | L (RUL) | Lung (LLL) |
| 8 | 16 | 16 | 100 | 2.04 | 1.82 | 89.2 | L (RUL) | Lymph node |
| 9 | 18.5 | 14.5 | 78.38 | 2.44 | 1.8 | 73.8 | L (LUL) | Bone |
| 10 | 21 | 21 | 100 | 5.14 | 3.99 | 77.6 | L (RML) | Lymph node |
| 11 | 21.5 | 21.5 | 100 | 4.75 | 4.04 | 85.1 | L (RLL) | Lung (LLL) |
| 12 | 29.2 | 29.2 | 100 | 12.38 | 10.55 | 85.2 | L (LLL) | Lymph node |
| 13 | 18 | 18 | 100 | 3.35 | 2.92 | 87.2 | L (RLL) | Lung (multiple) |
| 14 | 19.1 | 19.1 | 100 | 3.28 | 2.78 | 84.8 | Seg (LLL) | Lung (LUL) |
| 15 | 22.1 | 22.1 | 100 | 6.53 | 4.93 | 75.5 | L (RUL) | Lymph node |
| Death | | | | | | | | |
| 16 | 27.1 | 15 | 55.35 | 9.31 | 2.77 | 29.8† | Seg (RUL) | Pleura |
| 17 | 15.3 | 10 | 65.36 | 0.74 | 0.48* | 64.9 | L (LUL) | Brain |
| 18 | 12 | 12 | 100 | 0.87 | 0.64* | 73.6 | Seg (RLL) | Lymph node |
| 19 | 15.1 | 15.1 | 100 | 4.46 | 4.01 | 89.9 | L (LUL) | Lung (RUL) |
| 20 | 18.3 | 18.3 | 100 | 1.95 | 1.53 | 78.5 | Seg (LUL) | Lung (LUL) |
| 21 | 19.9 | 19.9 | 100 | 4.09 | 3.18 | 77.8 | L (RML) | Pleura |
| 22 | 22.2 | 22.2 | 100 | 6.33 | 4.69 | 74.1 | L (LLL) | Pleura |

Note.—Information in parentheses is excision cite. L = lobectomy, Seg = segmentectomy, RUL = right upper lobe, RML = right middle lobe, RLL = right lower lobe, LUL = left upper lobe, LLL = left lower lobe.

* Volume of solid component was less than 1.5 cm³.

† Percentage of solid volume was less than 63%.

factors and outcome measures. By using our custom software, automatic classification of nodules had excellent agreement with visual classification by radiologists; pure GGNs classified visually and by using software were associated with excellent prognosis with no recurrences or death observed. The uniformly excellent prognosis of pure GGNs after resection has been reported by several groups (24–26), and we are unaware of any cases of recurrence, even when nodules less than 3 cm of pure ground-glass composition are eventually found at pathologic examination to have invasive components (26).

Accurate segmentation of pulmonary nodules with or without ground-glass component is a challenging problem (27–31). In general, nodule segmentation is performed by using a combination of watershed and shape-analysis techniques; however, because these methods are edge-based, they cannot accurately delineate GGNs that typically share blurred margins with the surrounding lung parenchyma. Tan et al (31) have developed a probability-based method for segmentation of ground-glass nodules by using a Markov random model. By using this technique, the average overlap between computer and manual results for six nodules that contain ground-glass components was 60%. Kim et al (32) demonstrated that volumetric analysis was applicable for volume and mass measurement (12) of both pure and part-solid GGNs without measurement variation. In our study, we elected to segment nodules by using the mean FWHM of multiple density profile curves found by using CT

imaging, drawn through the center of each tumor, with recognition that this would be an imperfect but reproducible technique that likely underestimates the extent of peripheral ground glass in some cases of part-solid GGNs. Incorporation of a three-dimensional line filter in our software also allowed for the elimination of both contiguous and intralesional vessels that may artificially increase the calculated total tumor or solid tumor volume measurements, respectively.

Similar to previous studies (4,33–35), we found that for stage I adenocarcinoma, measurement of total tumor was associated less with prognostic factors and outcome than it was with measurements of the solid component. In our study, percentage of solid volume of 63% or greater was associated
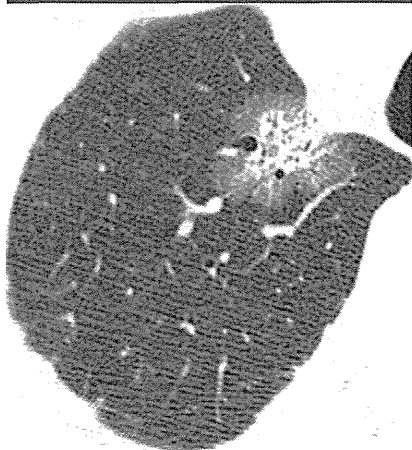
**Figure 6:** Thin-section CT image of a 27-mm nodule with multiple foci of solid components in a 65-year-old man who eventually died of recurrent disease. Volumetric measurements were total tumor volume, 9.31 cm³; solid tumor volume, 2.77 cm³; and percentage of solid tumor volume, 29.8%.

with the presence of pleural invasion; none of the four volumetric measurements were found to be associated with lymphatic or vascular invasion. This latter finding is discordant with results reported by Tsutani et al (33), who found that in 502 patients with clinical stage IA adenocarcinoma, solid tumor diameter was predictive of pleural, as well as of vascular and lymphatic invasion. Difference in results may be related to differences in the enrolled patient populations because our study included patients with pathologic stage I adenocarcinoma without lymph node metastases, and who therefore had a correspondingly lower prevalence of lymphatic invasion, vascular invasion, and pleural invasion compared with the population studied by Tsutani et al.

By using our volumetric automated computer-assisted analytic program, we found two volumetric measurements, solid volume of 1.5 cm³ or greater and percentage of solid volume of 63% or greater, to be independent indicators associated with recurrence and/or death in patients with stage I adenocarcinoma. These results are consistent with those of previous studies that also reported that features found

by using CT imaging, such as maximum diameter of the solid component (4,33) and ratio of maximum diameter of solid to ground-glass components exceeding 50% (2,36), can be associated with tumor recurrence after surgery. In our study, the two volumetric measurements were complementary, and used in combination they correctly identified 21 of 22 (95%) recurrent tumors. However, none of our evaluated two-dimensional measurements were found at multivariate analysis to be independent indicators associated with outcome; this lack of statistically significant results at multivariate analysis likely reflects the high degree of correlation between two-dimensional and volumetric variables and suggests that of the two quantitative sets, volumetric measurements may serve as better indicators associated with outcome. Compared with two-dimensional analysis that typically consists of tumor measurements on one or two images, volumetric analysis enables a more comprehensive and representative evaluation that may be particularly important for adenocarcinomas that have multiple foci of solid components.

Our study had several limitations. The study was retrospective in nature, and the relatively small number of enrolled patients may have resulted in inadequate statistical power to detect some CT features associated with prognosis. Results found in our study that had no statistically significant differences may have been caused by a true lack of differences or by the small sample size. Prospective studies with larger sample sizes will be needed to validate our results. Segmentation of subsolid nodules by using our custom software was imperfect with underestimation of the extent of peripheral ground glass. Given that ground glass is known to correspond to the lepidic noninvasive component of tumor, we chose not to perform manual edits so as to avoid the introduction of observer variability. Computer analysis of nodules was performed by only one operator who was required to select a tumor center point and draw an over-inclusive region of interest around the nodule before

automated volumetric measurements could be performed. Ideally, the inclusion of one or more additional operators would have allowed for assessment of the reproducibility of the computer-generated volumetric measurements. Finally, inconsistency in the types of operations may have negatively affected outcomes in some patients who underwent sublobar resection; there are currently two ongoing randomized trials in Japan and North America to address whether segmentectomy can replace lobectomy as standard treatment (1).

In conclusion, our results demonstrated that two volumetric measurements (solid volume of ≥1.5 cm³ and percentage of solid volume of ≥63%) are independent and complementary indicators associated with recurrence and/or death in patients with stage I adenocarcinoma. These results may have implications for determination of the optimal management of subsolid nodules.

## References

1. Travis WD, Brambilla E, Noguchi M, et al. International association for the study of lung cancer/american thoracic society/european respiratory society international multidisciplinary classification of lung adenocarcinoma. J Thorac Oncol 2011;6(2):244–285.

2. Ikehara M, Saito H, Yamada K, et al. Prognosis of small adenocarcinoma of the lung based on thin-section computed tomography and pathological preparations. J Comput Assist Tomogr 2008;32(3):426–431.

3. Nakazono T, Sakao Y, Yamaguchi K, Imai S, Kumazoe H, Kudo S. Subtypes of peripheral adenocarcinoma of the lung: dif-

ferentiation by thin-section CT. Eur Radiol 2005;15(8):1563–1568.

4. Sakao Y, Nakazono T, Tomimitsu S, et al. Lung adenocarcinoma can be subtyped according to tumor dimension by computed tomography mediastinal-window setting. Additional size criteria for clinical T1 adenocarcinoma. Eur J Cardiothorac Surg 2004;26(6):1211–1215.

5. Noguchi M. Stepwise progression of pulmonary adenocarcinoma—clinical and molecular implications. Cancer Metastasis Rev 2010;29(1):15–21.

6. Naidich DP, Bankier AA, MacMahon H, et al. Recommendations for the management of subsolid pulmonary nodules detected at CT: a statement from the Fleischner Society. Radiology 2013;266(1):304–317.

7. Yankelevitz DF, Reeves AP, Kostis WJ, Zhao B, Henschke CI. Small pulmonary nodules: volumetrically determined growth rates based on CT evaluation. Radiology 2000;217(1):251–256.

8. Ko JP, Rusinek H, Jacobs EL, et al. Small pulmonary nodules: volume measurement at chest CT—phantom study. Radiology 2003;228(3):864–870.

9. Das M, Mühlenbruch G, Katoh M, et al. Automated volumetry of solid pulmonary nodules in a phantom: accuracy across different CT scanner technologies. Invest Radiol 2007;42(5):297–302.

10. Marchianò A, Calabrò E, Civelli E, et al. Pulmonary nodules: volume repeatability at multidetector CT lung cancer screening. Radiology 2009;251(3):919–925.

11. Ko JP, Berman EJ, Kaur M, et al. Pulmonary Nodules: growth rate assessment in patients by using serial CT and three-dimensional volumetry. Radiology 2012;262(2):662–671.

12. de Hoop B, Gietema H, van de Vorst S, Murphy K, van Klaveren RJ, Prokop M. Pulmonary ground-glass nodules: increase in mass as an early indicator of growth. Radiology 2010;255(1):199–206.

13. Sato Y, Nakajima S, Shiraga N, et al. Three-dimensional multi-scale line filter for segmentation and visualization of curvilinear structures in medical images. Med Image Anal 1998;2(2):143–168.

14. Yanagawa M, Kuriyama K, Kunitomi Y, et al. One-dimensional quantitative evaluation of peripheral lung adenocarcinoma with or without ground-glass opacity on thin-section CT images using profile curves. Br J Radiol 2009;82(979):532–540.

15. Kuriyama K, Gamsu G, Stern RG, Cann CE, Herfkens RJ, Brundage BH. CT-determined pulmonary artery diameters in predicting pulmonary hypertension. Invest Radiol 1984;19(1):16–22.

16. Liu HL, Liu RR, Reeve DM, Shepard SJ, Willis CE. Measurement of CT radiation profile width using CR imaging plates. Med Phys 2005;32(9):2881–2887.

17. Pratt WK. Digital image processing. 4th ed. Los Altos, Calif: Wiley, 2007.

18. Yanagawa M, Tanaka Y, Kusumoto M, et al. Automated assessment of malignant degree of small peripheral adenocarcinomas using volumetric CT data: correlation with pathologic prognostic factors. Lung Cancer 2010;70(3):286–294.

19. Evangelou E, Kyzas PA, Trikalinos TA. Comparison of the diagnostic accuracy of lymphatic endothelium markers: Bayesian approach. Mod Pathol 2005;18(11):1490–1497.

20. Giatromanolaki A, Koukourakis MI, Theodossiou D, et al. Comparative evaluation of angiogenesis assessment with anti-factor-VIII and anti-CD31 immunostaining in non-small cell lung cancer. Clin Cancer Res 1997;3(12 Pt 1):2485–2492.

21. Maclure M, Willett WC. Misinterpretation and misuse of the kappa statistic. Am J Epidemiol 1987;126(2):161–169.

22. Gould MK, Donington J, Lynch WR, et al. Evaluation of individuals with pulmonary nodules: when is it lung cancer? Diagnosis and management of lung cancer, 3rd ed: American College of Chest Physicians evidence-based clinical practice guidelines. Chest 2013;143(5 Suppl):e93S–120S.

23. Arenas-Jiménez J. Measurement of solid component in part-solid lesions with a mediastinal window setting? Radiology 2013;268(1):305–306.

24. Nakamura H, Saji H, Ogata A, Saijo T, Okada S, Kato H. Lung cancer patients showing pure ground-glass opacity on computed tomography are good candidates for wedge resection. Lung Cancer 2004;44(1):61–68.

25. Park JH, Lee KS, Kim JH, et al. Malignant pure pulmonary ground-glass opacity nodules: prognostic implications. Korean J Radiol 2009;10(1):12–20.

26. Lim HJ, Ahn S, Lee KS, et al. Persistent pure ground-glass opacity lung nodules ≥ 10 mm in diameter at CT scan: histopathologic comparisons and prognostic implications. Chest 2013;144(4):1291–1299.

27. Revel MP, Lefort C, Bissery A, et al. Pulmonary nodules: preliminary experience with three-dimensional evaluation. Radiology 2004;231(2):459–466.

28. Zhao B, Reeves A, Yankelevitz D, Henshke C. Three-dimensional multi-criterion automatic segmentation of pulmonary nodules of helical computed tomography images. Opt Eng 1999;38(8):1340–1347.

29. Reeves AP, Chan AB, Yankelevitz DF, Henschke CI, Kressler B, Kostis WJ. On measuring the change in size of pulmonary nodules. IEEE Trans Med Imaging 2006;25(4):435–450.

30. Kauczor HU, Heitmann K, Heussel CP, Marwede D, Uthmann T, Thelen M. Automatic detection and quantification of ground-glass opacities on high-resolution CT using multiple neural networks: comparison with a density mask. AJR Am J Roentgenol 2000;175(5):1329–1334.

31. Tan Y, Schwartz LH, Zhao B. Segmentation of lung lesions on CT scans using watershed, active contours, and Markov random field. Med Phys 2013;40(4):043502.

32. Kim H, Park CM, Woo S, et al. Pure and part-solid pulmonary ground-glass nodules: measurement variability of volume and mass in nodules with a solid portion less than or equal to 5 mm. Radiology 2013;269(2):585–593.

33. Tsutani Y, Miyata Y, Nakayama H, et al. Prognostic significance of using solid versus whole tumor size on high-resolution computed tomography for predicting pathologic malignant grade of tumors in clinical stage IA lung adenocarcinoma: a multicenter study. J Thorac Cardiovasc Surg 2012;143(3):607–612.

34. Maeyashiki T, Suzuki K, Hattori A, Matsunaga T, Takamochi K, Oh S. The size of consolidation on thin-section computed tomography is a better predictor of survival than the maximum tumour dimension in resectable lung cancer. Eur J Cardiothorac Surg 2013;43(5):915–918.

35. Sakao Y, Miyamoto H, Sakuraba M, et al. Prognostic significance of a histologic subtype in small adenocarcinoma of the lung: the impact of nonbronchioloalveolar carcinoma components. Ann Thorac Surg 2007;83(1):209–214.

36. Hashizume T, Yamada K, Okamoto N, et al. Prognostic significance of thin-section CT scan findings in small-sized lung adenocarcinoma. Chest 2008;133(2):441–447.

ARTICLE IN PRESS

# Safety and tolerability of allogeneic dendritic cell vaccination with induction of Wilms tumor 1—specific T cells in a pediatric donor and pediatric patient with relapsed leukemia: a case report and review of the literature

SHOJI SAITO[1,2], RYU YANAGISAWA[1,2], KENTARO YOSHIKAWA[1,2],
YUMIKO HIGUCHI[1], TERUTSUGU KOYA[1], KIYOSHI YOSHIZAWA[1],
MIYUKI TANAKA[2], KAZUO SAKASHITA[2], TAKASHI KOBAYASHI[1],
TAKASHI KURATA[2], KOICHI HIRABAYASHI[2], YOZO NAKAZAWA[2],
MASAAKI SHIOHARA[2], YOSHIKAZU YONEMITSU[3], MASATO OKAMOTO[4],
HARUO SUGIYAMA[5], KENICHI KOIKE[2] & SHIGETAKA SHIMODAIRA[1]

[1]Center for Advanced Cell Therapy, Shinshu University Hospital, Matsumoto, Japan, [2]Department of Pediatrics,
Shinshu University School of Medicine, Matsumoto, Japan, [3]R&D Laboratory for Innovative Biotherapeutics, Kyushu
University Graduate School of Pharmaceutical Sciences, Fukuoka, Japan, [4]Department of Advanced
Immunotherapeutics, Kitasato University School of Pharmacy, Tokyo, Japan, and [5]Functional Diagnostic Science,
Osaka University Graduate School of Medicine, Osaka, Japan

## Abstract
A 15-year-old girl with acute lymphoblastic leukemia received allogeneic dendritic cell vaccination, pulsed with Wilms tumor 1 (WT1) peptide, after her third hematopoietic stem cell transplantation (HSCT). The vaccines were generated from the third HSCT donor, who was her younger sister, age 12 years. The patient received 14 vaccines and had no graft-versus-host disease or systemic adverse effect, aside from grade 2 skin reaction at the injection site. WT1-specific immune responses were detected after vaccination by both WT1-tetramer analysis and enzyme-linked immunosorbent spot assay. This strategy may be safe, tolerable and even feasible for patients with a relapse after HSCT.

Key Words: dendritic cells, ELISPOT, HSCT, tetramer analysis, Wilms tumor 1

## Introduction

The outcome of patients with relapsed leukemia after allogeneic hematopoietic stem cell transplantation (HSCT) is discouraging and indicates an urgent need for new therapies [1]. Donor lymphocyte infusion (DLI) has been proposed to overcome leukemic relapse after HSCT by boosting graft-versus-leukemia effect. However, DLI provokes unmanageable graft-versus-host disease (GVHD) because many allogeneic antigens are targeted by donor T cells [2].

Leukemic antigen-specific autologous dendritic cell (DC)-based vaccination for hematological malignancies is currently explored to avoid off-target effects [3,4]. The autologous DC therapy requires the production of DC vaccines from patient-derived

peripheral blood mononuclear cells (PBMCs) through the use of leukapheresis. Although healthy donor-derived PBMCs may be available to generate the allogeneic DC vaccines in the patients who received HSCT, little has been reported on the safety and tolerability of the production and administration of donor-derived DCs for the donor and recipient. Additionally, the induction of leukemic antigen-specific T cells by allogeneic DC vaccines remains unclear.

Thus, we conducted a phase I clinical trial to test the safety and tolerability of Wilms tumor 1 (WT1)-specific allogeneic DC vaccination for pediatric patients with relapsed leukemia after HSCT. We report the results from the first patient who completed the allogeneic DC vaccination.

2   S. Saito et al.

## Methods

### Patients

This clinical trial (UMIN: 000002105) was approved by the institutional review board of the Shinshu University School of Medicine. Written informed consent was obtained from patients over 12 years of age, HSCT donors and their parents, according to the *Helsinki Declaration*. Adverse effects were graded by use of the National Cancer Institute's Common Toxicity Criteria version 3.

### Preparation of allogeneic DC vaccine

Mature DCs (mDCs) were generated under Good Manufacturing Practice conditions and cryopreserved in liquid nitrogen as described previously [5], with some modification. Briefly, a PBMC-rich fraction was obtained from the HSCT donor by means of leukapheresis with the use of the COM.TEC, cell separator (Fresenius Kabi Japan K.K., Tokyo, Japan). The PBMCs were isolated from leukapheresis products by use of Ficoll-Hypaque gradient-density centrifugation as described previously and placed into 100-mm plastic tissue-culture plates (Becton Dickinson Labware, Franklin Lakes, NJ, USA) in AIM-V medium (Gibco, Gaithersburg, MD, USA). After 30 min of incubation, nonadherent cells were removed and adherent cells were cultured in AIM-V medium. On the next day, 50 ng/mL of granulocyte-macrophage colony-stimulating factor (Gentaur, Brussels, Belgium) and 50 ng/mL of interleukin-4 (R&D Systems Inc, Minneapolis, MN, USA) were added to generate immature DCs. After 5 days of culture, immature DCs were subsequently stimulated with 10 μg/mL of OK-432 (streptococcal preparation, Chugai Pharmaceutical Co, Ltd, Tokyo, Japan) and 50 ng/mL of prostaglandin E2 (Daiichi Fine Chemical Co, Ltd, Toyama, Japan) for 24 hours to generate mDCs. The mDCs were cryopreserved and kept in liquid nitrogen until the day of administration. Cell culture supernatant is collected for sterility testing at the time of freezing. Surface molecules expressed by the DCs were determined by means of flow cytometry. The phenotype cluster of differentiation (CD) $14^-$, human leukocyte antigen (HLA)-DR$^+$, HLA-ABC$^+$, CD80$^+$, CD83$^+$, CD86$^+$, CD40$^+$ and CCR7$^+$ were defined as mDCs [6].

For each vaccination, an aliquot of frozen mDCs was thawed just before clinical use and loaded with 100 μg/mL of HLA-A*24:02-restricted modified WT1 peptide (CYTWNQML, residue 235−243) and 1−2KE of OK-432 adjuvant.

### Release criteria

Release criteria for administering the DC vaccine to patients include purity >90%, viability >80%, mDC phenotype, negative culture for bacteria and fungi after 14 days, endotoxin testing $\leq$ 0.05 EU/mL and negative result for mycoplasma.

### Tetramer staining

Unstimulated PBMCs were stained with phycoerythrin-conjugated human immunodeficiency virus/HLA-A*24:02 tetramer as a negative control for phycoerythrin-conjugated WT1-modified peptide/HLA-A*24:02 tetramer (MBL, Medical & Biological Laboratories Co, Ltd, Nagoya, Japan), allophycocyanin-conjugated anti-human CD3 monoclonal antibodies (mAb) (Biolegend, San Diego, CA, USA) and fluorescein isothiocyanate−conjugated anti-human CD8 mAb (Beckman Coulter, Miami, FL, USA) and then were analyzed by means of flow cytometry (FACSCalibur, BD Biosciences, San Jose, CA, USA).

### Enzyme-linked immunosorbent spot assay

The enzyme-linked immunosorbent spot (ELISPOT) assay was performed to examine WT1-specific interferon (INF)-γ production by CD8$^+$ T cells by use of the human interferon (IFN)-γ ELISpot PLUS kit (Mabtech, Nacka Strand, Sweden) according to the manufacturer's instructions. Briefly, the CD8$^+$ cells were isolated from the patient's PBMCs at each time point through the use of microbead-conjugated CD8 mAbs (Miltenyi Biotec, San Diego, CA, USA) and were then cultured ($5 \times 10^3$ cells/well) in the presence of WT1$_{235-243}$ peptide and the CD8$^-$ cells from the PBMCs at the time of initial vaccination as stimulator cells. After 20 hours of incubation, the spots were counted by an automated ELISPOT reader (AID EliSpot Reader Classic ELR 07, Autoimmun Diagnostika GmbH, Strassberg, Germany).

## Case report

### Transplantations and lymphocyte infusions

A 12-year-old girl was diagnosed with B-precursor acute lymphoblastic leukemia. She underwent allogeneic bone marrow transplantation from her mother (HLA 8/8 allele-match) in first complete remission (CR) (first HSCT, Figure 1). The engraftment was successful, but she had a hematological relapse 11 months after this first HSCT. A combination of chemotherapy and two sessions of donor lymphocyte infusion (DLI) did not induce long-term remission. Consequently, she was transplanted with peripheral blood stem cells from the same donor (second HSCT, Figure 1) and successfully achieved a third CR. However, a third hematological relapse occurred
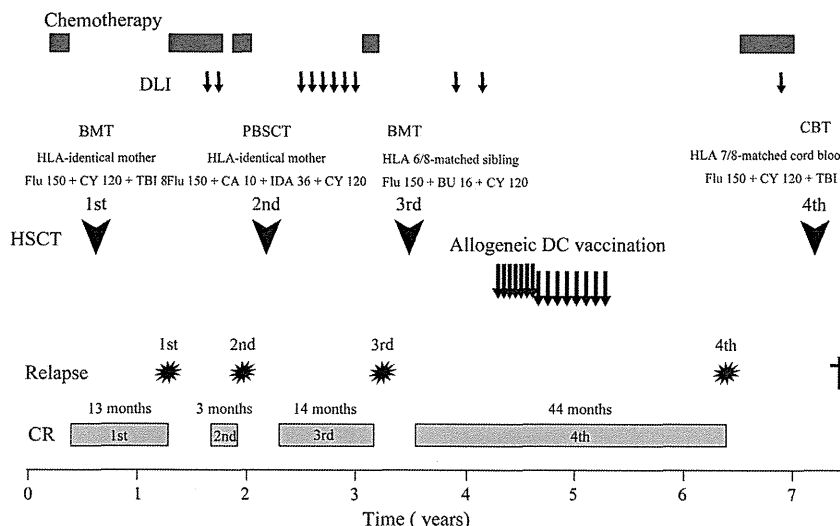
Figure 1. Clinical course of the patient. Allogeneic DC vaccination initiated 13 months after the third HSCT. BMT, bone marrow transplantation; CBT, cord blood transplantation; Flu 150, fludarabine 150 mg/m$^2$; CY 120, cyclophosphamide 120 mg/kg; TBI 8, total body irradiation 8 Gy; CA 10, cytarabine 10 g/m$^2$; IDA, idarubicin 36 mg/m$^2$; BU 16, busulfan (intravenously) 16 mg/kg.

14 months after the second HSCT. Therefore, she received bone marrow transplantation from her HLA 6/8—matched (A and DR alleles mismatched) sister in the third relapse (third HSCT, Figure 1). She successfully achieved neutrophil engraftment on day 16 and a fourth CR on 55. On day 50, she had grade 2 acute GVHD, but her condition was promptly improved by increasing the dose of tacrolimus. All immunosuppressants were discontinued by day 75. Additionally, she received two sessions of prophylactic DLIs (0.1 or 1 × 10$^6$ CD3$^+$ cells/kg) from her third HSCT donor on days 105 and 245.

### Allogeneic DC vaccination

At 15 years of age, the patient was referred to our center for enrollment in a clinical study on allogeneic DC vaccination. She and her 12-year-old sister (third HSCT donor) had identical HLA-A*24:02 alleles. At the time of the third relapse, WT1 messenger RNA (mRNA) was overexpressed in the bone marrow (BM) (1.6 × 10$^4$ copies/μg RNA) and peripheral blood (PB) (1.5 × 10$^3$ copies/μg RNA), which included 1% and 42.6% blasts, respectively (Supplementary Figure 1). Therefore, they met the eligibility criteria for the clinical trial (UMIN: 000002105). Written informed consent was obtained from the patient, the third HSCT donor and their parents.

PBMCs were obtained from the donor by means of leukapheresis. Leukapheresis elicited no adverse effect, except for grade 1 nausea in the donor. Mature DCs were produced at the cell processing center of the Shinshu University Hospital under Good Manufacturing Practice conditions. Finally, 15

doses of DC vaccines (1 × 10$^7$ cells/dose) were generated from the single leukapheresis.

Allogeneic DC vaccination was started 13 months after the third HSCT (Figure 1). The patient maintained a fourth CR with no evidence of GVHD without receiving any immunosuppressive therapy at the time of initial vaccination. First, the patient received seven intradermal injections of DC vaccines pulsed with WT1$_{235-243}$ peptide, each dose given every 2 weeks. Because this initial immunization did not cause severe adverse effects, except for a grade 2 injection site reaction, the patient received seven additional vaccinations, given every 4 weeks. These booster vaccinations were well tolerated, aside from itching and grade 2 local erythema and vesicles at the injection sites. After the 14th vaccination, the patient maintained complete hematological remission with complete donor chimerism. Therefore, vaccination was discontinued at the request of the patient and her parents. No vaccination-related GVHD, pancytopenia or other systematic adverse effects developed during the 14 sessions of vaccination. Additionally, no immunosuppressive therapy was given during the vaccination.

WT1 mRNA expression in peripheral blood and recipient-specific chimerism in bone marrow were sequentially measured for detecting minimal residual disease during vaccination (Supplementary Figure 1). Both minimal residual disease markers disappeared before commencing the vaccination and were maintained below detectable levels during the vaccination.

Unfortunately, a fourth relapse occurred 44 months after the third HSCT, which was 14 months after the final vaccination. At the time of the fourth
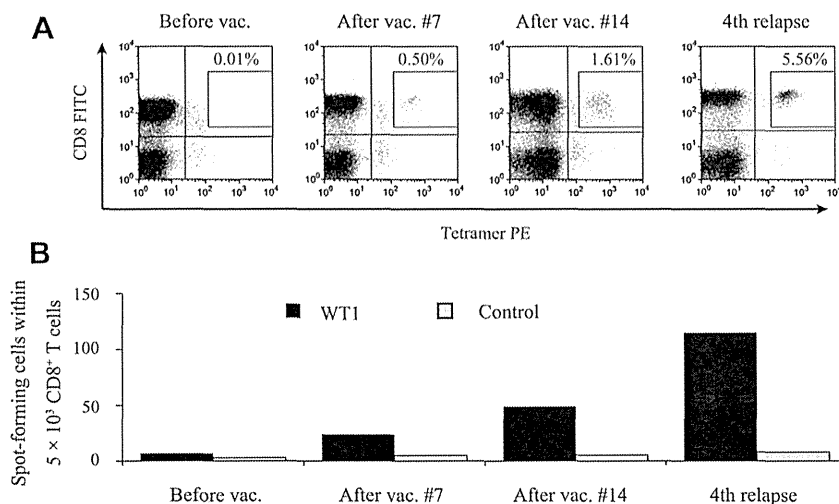
Figure 2. Impact of allogeneic DC vaccination on (vac.) (A) WT1-specific tetramer CD8$^+$ T-cell frequencies and (B) INF-$\gamma$ production. (A) Tetramer staining of CD8$^+$ T cells. WT1$_{235-243}$ tetramer$^+$ CD8$^+$ T cells were detected after allogeneic DC vaccination. Shown are the frequencies of CD8$^+$ and tetramer$^+$ cells in the CD3$^+$ population. Numbers indicate the percentages of tetramer-positive cells within the CD8$^+$ population. (B) ELISPOT assays of the CD8$^+$ T cells isolated from the patient's PBMCs. WT1-specific IFN-$\gamma$ secretion by CD8$^+$ T cells increased after vaccination. Histogram bars represent mean values from duplicate wells at each time point. White and black bars indicate IFN-$\gamma$ secretion by CD8$^+$ T cells stimulated with human immunodeficiency virus (HIV) peptide and WT1 peptide, respectively.

relapse, WT1 mRNA was similarly overexpressed in BM (1.1 × 10$^4$ copies/μg RNA) and PB (1.3 × 10$^3$ copies/μg RNA), similar to that in the third relapse, which included 80.8% and 33.0% leukemic blasts, respectively (Supplementary Figure 1). The patient did not achieve hematological remission after chemotherapy and a single dose of DLI. Eight months after the fourth relapse, she received an HLA 7/8—matched transplant from unrelated cord blood (fourth HSCT, Figure 1). However, she died of invasive pulmonary aspergillosis 38 days after this transplant.

We closed the clinical trial only with this case because of difficulty in recruiting eligible patients.

*Induction of WT1-specific immune response*

CD8$^+$ tetramer$^+$ T cells were detected in the patient after the seven sessions of initial immunization, and they increased in number after the seven sessions of booster immunization (Figure 2A).

Furthermore, WT1-specific INF-$\gamma$—producing CD8$^+$ T cells were also detected after the initial immunization and were definitely increased by the booster vaccinations (Figure 2B). Interestingly, the numbers of WT1-specific INF-$\gamma$—producing CD8$^+$ T cells reached maximum values at the fourth relapse.

To determine the reasons why these functional WT1-specific T cells failed to prevent a relapse, we isolated the relapsed leukemia cells from the PBMCs by use of microbead-conjugated CD34 mAbs (Miltenyi Biotec) and performed HLA typing by use of the short-tandem repeat—polymerase chain reaction

method. HLA typing was also performed on the CD3$^+$ cells isolated from the PBMCs obtained during complete remission. HLA genotyping of the CD34$^+$ leukemia cells from both third and fourth relapses showed a homozygous HLA-A*24:02/-allele, consistent with the CD3$^+$ cells.

## Discussion

This study describes the treatment of the youngest donor and recipient for allogeneic DC vaccination. We successfully generated 15 doses of DC vaccine (1 × 10$^7$ cells/dose) safely from a 12-year-old, healthy donor, with a single leukapheresis session. The 14 doses of allogeneic DC vaccination pulsed with WT1$_{235-243}$ peptide were all safe and well tolerated by the 15-year-old patient, without adverse effects except for a grade 2 local reaction. A literature review identified six patients with hematological malignancies who received donor-derived allogeneic DC vaccines after HSCT, including this present case (Table I). It is noteworthy that none of them had GVHD or systemic adverse events after allogeneic DC vaccination pulsed with tumor lysate [7] or WT1 peptide [8]. Together, previous and current reports suggest that leukemia antigen—specific allogeneic DC vaccination should be safe and well-tolerated by post-transplant relapsed patients, even in pediatric patients who received allografts from their sibling donors.

WT1-specific immune responses were markedly detected after vaccination by both WT1-tetramer analysis and ELISPOT assay in our patient. WT1 antigen has been considered a promising target for